NEUROTECHNOLOGY

Microstructured thin-film electrode technology enables proof of concept of scalable, soft auditory brainstem implants

Nicolas Vachicouras[1]*, Osama Tarabichi[2]*, Vivek V. Kanumuri[2]*, Christina M. Tringides[1]†, Jennifer Macron[1], Florian Fallegger[1], Yohann Thenaisie[1], Lorenz Epprecht[2], Stephen McInturff[2], Ahad A. Qureshi[2], Valentina Paggi[1], Martin W. Kuklinski[2], M. Christian Brown[2], Daniel J. Lee[2‡], Stéphanie P. Lacour[1‡]

Auditory brainstem implants (ABIs) provide sound awareness to deaf individuals who are not candidates for the cochlear implant. The ABI electrode array rests on the surface of the cochlear nucleus (CN) in the brainstem and delivers multichannel electrical stimulation. The complex anatomy and physiology of the CN, together with poor spatial selectivity of electrical stimulation and inherent stiffness of contemporary multichannel arrays, leads to only modest auditory outcomes among ABI users. Here, we hypothesized that a soft ABI could enhance biomechanical compatibility with the curved CN surface. We developed implantable ABIs that are compatible with surgical handling, conform to the curvature of the CN after placement, and deliver efficient electrical stimulation. The soft ABI array design relies on precise microstructuring of plastic-metal-plastic multilayers to enable mechanical compliance, patterning, and electrical function. We fabricated soft ABIs to the scale of mouse and human CN and validated them in vitro. Experiments in mice demonstrated that these implants reliably evoked auditory neural activity over 1 month in vivo. Evaluation in human cadaveric models confirmed compatibility after insertion using an endoscopic-assisted craniotomy surgery, ease of array positioning, and robustness and reliability of the soft electrodes. This neurotechnology offers an opportunity to treat deafness in patients who are not candidates for the cochlear implant, and the design and manufacturing principles are broadly applicable to implantable soft bioelectronics throughout the central and peripheral nervous system.

INTRODUCTION

The auditory brainstem implant (ABI) provides sound sensations to patients who are deaf and who have damaged or absent cochlear or cochlear nerve anatomy (1, 2). Most ABI users have neurofibromatosis type 2 (NF2), an autosomal dominant genetic syndrome associated with the formation of multiple brain and spinal neoplasms, including bilateral vestibular schwannomas. Growth or clinical management of these intracranial tumors results in damage to cochlear nerves and profound hearing loss. The ABI has also been studied in several clinical trials in children with congenital aplasia of the cochlea or cochlear nerve, or in patients with scarring of the cochlea following trauma, otosclerosis, or meningitis (3, 4). The ABI bypasses the auditory periphery to evoke sound sensations using electrical stimulation of the cochlear nucleus (CN). The CN is a <25-mm^3 structure in the brainstem (5, 6) that receives inputs from the cochlear nerve (7, 8). To stimulate the CN, the ABI uses a planar electrode array with up to 21 contacts that is placed during a posterior fossa craniotomy. Unlike

the majority of users of the cochlear implant, however, most ABI users do not achieve open-set comprehension of speech and are limited to sound awareness that assists in lip reading (2, 9).

One factor that may contribute to poor outcomes is the mechanical mismatch between the stiff ABI array and the soft and curvilinear underlying brainstem. This situation almost certainly leads to poor electrode contact with neural structures, thus requiring higher currents to stimulate auditory neurons and leading to consequent activation of nearby non-auditory areas (10). Side effects observed by ABI users include transitory dizziness, tingling sensations, facial twitching, and pain; the electrodes producing these effects must be turned off, reducing the number of auditory channels (11). Recent advances in soft bioelectronics have produced neural implants with greater conformability, narrowing the biomechanical mismatch between man-made implants and soft neural tissues (12, 13). The use of soft and elastic materials also opens the design path for implants that can accommodate micro- and macroscopic movements of neural tissue secondary to blood and cerebrospinal fluid flow, respiration, or head and neck movements (14, 15). A critical challenge when designing soft electrode implants is the patterning of robust, elastic, and highly conducting wires to interface the electrodes (in contact with neural tissue) with an implantable pulse generator. Typical strategies involve designs of meandering paths (16, 17), structured materials (18), and the use of inherently stretchable materials, such as micro- and nanocomposites that form percolating pathways (19).

In this study, we explored how advances in thin-film bioelectronic structures combined with soft materials can help in revising the design of the clinical ABIs (20–24). Plastic and elastic polymers such as polyimide (PI) and silicone, respectively, and thin metal films are routinely processed and machined using microfabrication technology (25–27).

Translational demonstrations and U.S. FDA (Food and Drug Administration)–approved devices using these materials in various neuroprosthetic applications motivated their use in this study (*28–30*). We designed, fabricated, and tested a soft multichannel ABI array with better biomechanical match between the array and the curved brainstem surface than existing systems. We engineered and defined stretchable metallic tracks (leads) from strain relief patterns and thin-film multilayers to carry electrical pulses to soft electrode coatings with efficient charge injection. We scaled the array to the size of a human ABI and verified the feasibility of surgical implantation onto the CN of a cadaveric specimen. Our microtechnology also allows for scaling down the design to the CN of a mouse, which we used as a model to validate the function and durability of the soft ABIs in vivo.

RESULTS

Design of conformable ABI arrays

The design process starts with the analysis of the in vivo environment. The ABI is to be inserted in the lateral sulcus of the fourth ventricle (Fig. 1, A and B) and placed on the surface of the dorsal CN (DCN). The radius of curvature of the DCN is about 3 mm in human (Fig. 1C). Current clinical ABIs (Fig. 1D) that use rigid electrode paddles poorly conform this small and curvilinear surface (Fig. 1E and fig. S1). Some of the electrodes do not interface the DCN. Electrical current spread and subsequent nonselective stimulation of neighboring tissue reduce the efficacy of the ABI (Fig. 1F and fig. S2). We hypothesize that the introduction of a soft, conformable design of the ABI will improve the implant-tissue interface. Then, the soft implant nicely wraps the surface of the DCN (Fig. 1E) and ensures a larger volume of the DCN that is activated with minimized losses of the injected current (Fig. 1G).

The conformable ABI is composed of an electrode array and elastic interconnects (Fig. 1H and fig. S3). Electrode contacts are made of a stretchable platinum-silicone composite (Fig. 1I), and the interconnects consist of microstructured multilayers of polyimide/platinum/polyimide (PI/Pt/PI) (2.2 μm in thickness) (Fig. 1J). The ABI is further embedded in a silicone membrane (200 μm in thickness).

The interconnects consist of long and narrow metallic tracks embedded in the bulk, elastomeric structure of the im-

plant. Their anisotropic layout and critical role in the function of the implant require careful design to guarantee mechanical compliance, robustness, and electrical continuity. The technique we used to fabricate these interconnects involved the microstructuring of hexagonally arranged Y-shaped cuts (figs. S3 and S4) that were previously
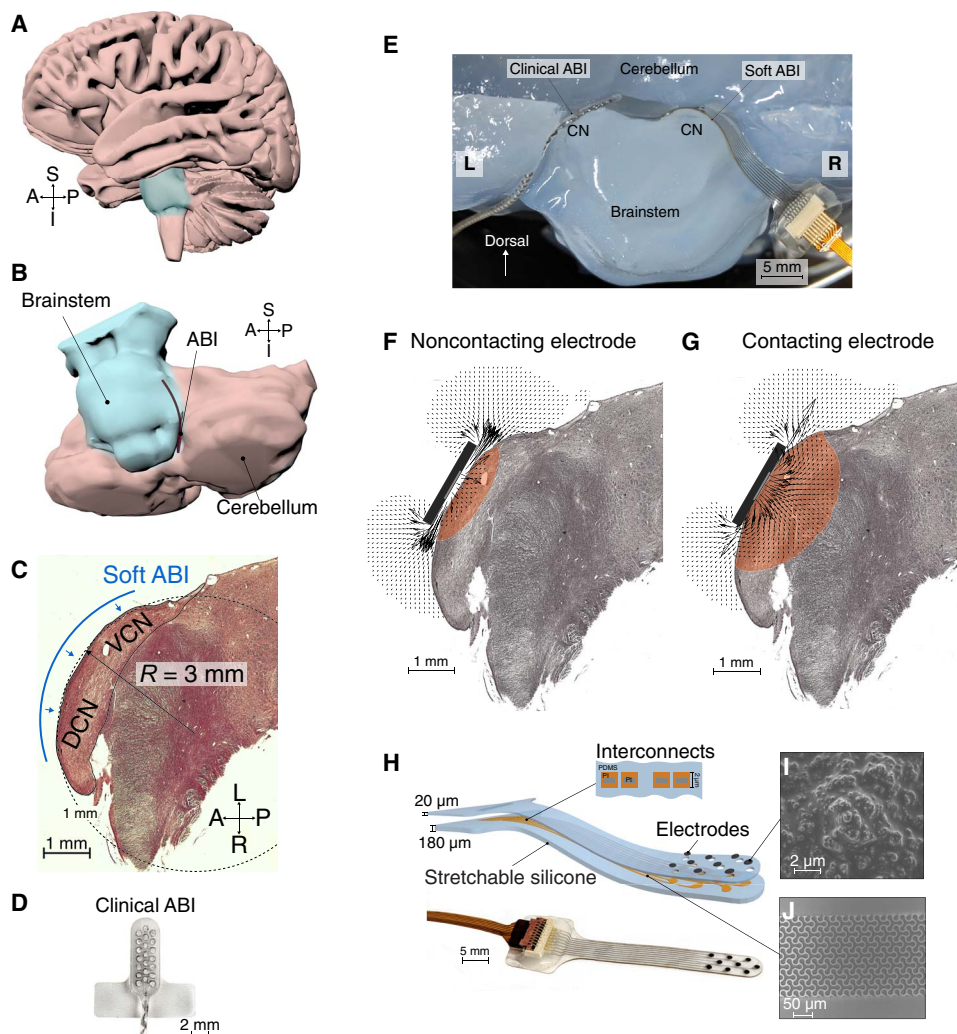
Fig. 1. Soft ABI electrode arrays conform to the curvature of the CN unlike the rigid electrode array of the clinical ABI. (**A**) Lateral view of an MRI reconstruction of the human brain with the brainstem shaded (blue). (**B**) Expanded view of the boxed region in (A), showing the position of the ABI electrode array between the cerebellum and the brainstem, in the lateral recess of the fourth ventricle. (**C**) Axial histological section of the brainstem with the dorsal and ventral subdivisions of the cochlear nucleus (DCN and VCN). The blue curve represents the soft electrode array conforming to the curved surface of the CN. The radius of curvature of the DCN (*R*) for this particular histological section was measured as 3 mm. (**D**) Photograph of one of the ABI electrode arrays currently in clinical use (Cochlear Ltd.). (**E**) Photograph showing the soft ABI conforming and the rigid clinical array not conforming to the curved surfaces of the right and left model DCNs, respectively. The agarose gel model is based on a 3D MRI reconstruction of the human brainstem. (**F**) Simulation results showing current density (black arrows) spreading in the cerebrospinal fluid and neural tissue upon stimulation (100 μA) using an electrode from a clinical ABI not completely in contact with the CN (left) and (**G**) an electrode from a soft ABI in contact with the CN (right). The colored surface shows an estimate of the tissue activation in both cases. Methodology is detailed in the "Simulation of cochlear nucleus electrical stimulation (surface of tissue activated)" section in the Supplementary Materials. (**H**) Top: Schematic representation of the soft ABI, a microstructured multilayer of PI and platinum forming the interconnects that are encapsulated between two layers of stretchable silicone. The electrodes sites are coated with a Pt-PDMS composite to decrease their impedance. Bottom: Photograph of the device with its connector. Scanning electron microscopy image of (**I**) the Pt-PDMS composite on the ABI electrode and (**J**) the microstructured multilayer in the interconnects. DCN, dorsal CN; VCN, ventral CN; S, superior; I, inferior; A, anterior; P, posterior; L, left; R, right.

shown to allow for isotropic stretchability in millimeter-sized plastic sheets (31). We further optimized these shapes by smoothing the edges of the Y pattern and embedding them on a microscopic multi-layered stack of PI/Pt/PI (~2.2 μm thick). These smoothed microstructures are geometrically defined by three parameters (Fig. 2A): the length of the branch, a; the radius of the circle at the tips, r; and the horizontal distance between two motifs, L (see the "Geometric construction of Y-shape pattern" section, fig. S5, and table S2 in the Supplementary Materials for a description). All microstructured tracks were embedded in silicone rubber (200 μm thick).

Finite element modeling of strain distribution and a corresponding photograph of the optimized structure highlighted the engineered strain relief mechanism (Fig. 2B). Calculations and samples were prepared at the macroscale for ease of manipulation. As the PI structure is stretched, the PI ligaments deflect out of plane, thereby locally relieving strain (18, 32). This was confirmed by the finite element analysis (FEA) model, which revealed that the maximum local strain was lower than the applied strain.

The Y-shaped design must also meet a mechanical and an electrical compromise. Narrow and open Y meshes are most compliant but at the expense of high electrical resistance of the structured tracks. We computed the maximal local strain and relative electrical resistance of patterns prepared with a range of a and r upon applied uniaxial strain of 10% (Fig. 2C and table S3).

We aimed for design parameters compatible with a maximum increase in electrical resistance of magnitude 10 (fig. S6 to S8), critical dimensions compatible with standard ultraviolet lithography on plastic foil (critical dimension <5 μm; fig. S9), and the lowest local strain possible. Three examples (designs 1, 2, and 3) are displayed in Fig. 2 (C and D) with arbitrarily set pattern pitch of $L = 26$ μm. We found that design 3 ($a = 16$ μm and $r = 5.5$ μm) offered the best design trade-off between maximum local strain and relative resistance (Fig. 2C) and displayed the lowest increase in resistance after 1000 strain cycles (Fig. 2D). The lithographic patterning of the Y-shaped structures provides a versatile method to pattern conductive tracks down to a width of 20 μm (figs. S10 and S11), which is the smallest track width geometrically allowed by the selected Y-shaped motifs' parameters (see the "Analytical expression of minimum track width" section in the Supplementary Materials).

We next compared the compliance and electromechanical response of bulk PDMS (polydimethylsiloxane), plain (nonstructured), and Y-shaped PI/Pt/PI tracks embedded in PDMS upon tensile deformation. Tracks prepared with Y-shaped microstructure displayed surprising deformability and stability compared to plain tracks. Y-shaped metallic tracks (200 μm wide and 17 mm long) mechanically failed at 80% tensile strain but did not fail electrically, whereas plain tracks of identical geometry failed both mechanically and electrically at only 3% applied strain (Fig. 2E and fig. S12). These improved mechanical characteristics were observed even for track widths down to 20 μm (fig. S13). Moreover, Fig. 2F demonstrates that the microstructure minimally affects the mechanical properties of the PDMS carrier in terms of apparent elastic modulus and fracture strain (fig. S14).

We next completed fatigue testing (1 million cycles, 10% applied strain) of the microstructured tracks (Fig. 1G). The microstructured tracks embedded in PDMS did not fail and showed an increase in resistance, from 8 to 45% across eight tracks (average 18 ± 12%) (Fig. 2G). Recommendations for clinical cochlear implants and ABIs [International Organization for Standardization (ISO) 45502-2-3:2010 standard] advise stability of the devices over 100,000 cycles, which is

an estimate of the number of flexural stress cycles that might occur after implantation on the electrode leads (33). The compliance and mechanical properties of the soft ABI are distinct from those of existing clinical devices. Therefore, we selected uniaxial stretching (10% applied strain) over bending to assess the integrity of the soft ABIs over mechanical stress and monitored electrical continuity of the tracks over time. We evaluated the ability of the microstructured tracks embedded in PDMS to conform to curvilinear surfaces. We found that the overall conformability of the soft membrane only depended on the PDMS, the thin tracks being mechanically transparent (Fig. 2H and fig. S15).

Electrochemical characterization of the soft electrodes
To enable efficient delivery of electrical pulses to neighboring neural tissue, electrodes interfaced to the microstructured tracks were coated with a soft composite material (12). We characterized the impedance of the combined interconnect and composite coating using electrochemical impedance spectroscopy (EIS). In phosphate-buffered saline (PBS), the average impedance at 1 kHz was 5.78 ± 0.62 kilohms ($n = 18$, 0.385 mm² surface area; Fig. 2I). The flat impedance spectrum in the 100- to 100-kHz frequency range suggested that the coating roughness successfully decreased the interfacial impedance.

A typical voltage transient response to a biphasic current pulse (1 mA, 300-μs pulse, a typical ABI stimulation current), recorded in PBS, is presented in Fig. 2J. This further demonstrates the suitability of soft and microfabricated neural leads to deliver safe and efficient current stimulation (Fig. 1G).

Cadaveric evaluation of the conformable ABI
We implemented soft neurotechnology to design and fabricate a soft ABI array and assessed its ability to conform to the curvature of the human CN. The soft ABI array had identical dimensions to current clinical devices used in humans (fig. S16). We first tested the device on agarose models of the human brainstem and CN, which were fabricated from three-dimensional (3D) magnetic resonance imaging (MRI) reconstructions (Fig. 1F). The CN had a radius of curvature of 2.85 ± 0.5 mm ($n = 3$ CN, histological reconstructions of the human DCN; fig. S17). The 200-μm-thick soft array conformed well to anatomic curvatures down to 2.8 mm (see the "DCN curvature estimation from histological specimens" section in Materials and Methods).

Surgical insertion of the soft ABI array was then assessed in cadaveric models following standard clinical procedures. A posterior fossa craniotomy was performed using either a retrosigmoid and/or translabyrinthine approach to visualize the cerebellum, brainstem, lower cranial nerves, and choroid plexus. The human CN is not directly visualized during surgery, and accurate placement relies on the identification of indirect landmarks and electrophysiology. We compared surgical insertion of a clinical ABI (movie S1) and a soft ABI array (movie S2) in terms of ease of handling and positioning and removal from the lateral recess of the fourth ventricle (key landmark for the CN) (Fig. 3, A and B). We found that the soft ABI array was difficult to insert though the lateral recess of the fourth ventricle, although the target was reached in all specimens. We next modified the soft ABI design to account for repeated positioning of the array that is often required during surgery to optimize the electrophysiological responses. We implemented a temporary guide affixed to the back (non-electrode side) of the array. The guide is prepared with a hydrosoluble polymer, poly(vinyl alcohol) (PVA), that temporarily stiffens the tip of the implant (Fig. 3C) and helps with handling and

Fig. 2. Electromechanical characteristics of stretchable materials used in the construction of soft ABI implants. (**A**) Micrograph of the Y-shaped motifs in a microstructured track. The red insets indicate the three independent geometrical parameters, *a*, *r*, and *L*, as well as the critical dimension (CD). (**B**) Mechanical simulation showing the local strain resulting from an applied strain (ε_{app}) of 20% on a sheet of structured PI (left), and a photograph of a real sample stretched at 20% strain (right). (**C**) Graphical representation of the optimization study. Each dot represents a Y-shaped pattern with a different combination of parameters *a* and *r* (right). Three different designs are illustrated. (**D**) Change in electrical resistance as a function of stretching (10% applied strain) for 1000 cycles on microfabricated samples with all three designs. The study used PI/Pt/PI interconnects embedded in PDMS. (**E**) A microfabricated sample with (blue) and without (purple) microstructured Y-shaped cuts was stretched up to failure (indicated by a cross). The resistance is shown as a function of the applied strain (*n* = 2 samples, each with eight tracks 200 μm wide). (**F**) Measured force as a function of applied strain for the same samples as in (E). The red curve shows a free-standing sample of PDMS without embedded interconnects for comparison (*n* = 2 samples). (**G**) A sample was reversibly stretched to 10% for 1 million (1M) cycles. The graph shows the relative change in resistance as a function of the number of cycles. (**H**) Graph showing the theoretical thicknesses for which a rectangular sample of plain PDMS can conform to a specific wet cylinder of radius R. The left graph contains experimental dots representing samples of plain

PDMS. The right graph contains experimental dots representing samples of 2-μm-thick microstructured multilayers of PI and platinum encapsulated between two layers of PDMS. The inset on the far right shows a photograph of an experimental sample of microstructured PI/Pt/PI embedded in 217-μm-thick PDMS conforming to an agarose cylinder of 4 mm in radius (arrow). (**I**) Electrical impedance norm (top) and phase (bottom) of the soft ABI electrodes measured in PBS as a function of frequency. Inset: Photograph of the microfabricated electrode contacts of the soft ABI. (**J**) Voltage measured on the soft ABI upon stimulation in PBS with a 1-mA biphasic current pulse (300 μm in width) at 100 Hz (*n* = 2 samples, with nine electrodes per device) using an external stimulator (Isolated Pulse Stimulator Model 2100, AM Systems). Shaded areas denote SD.
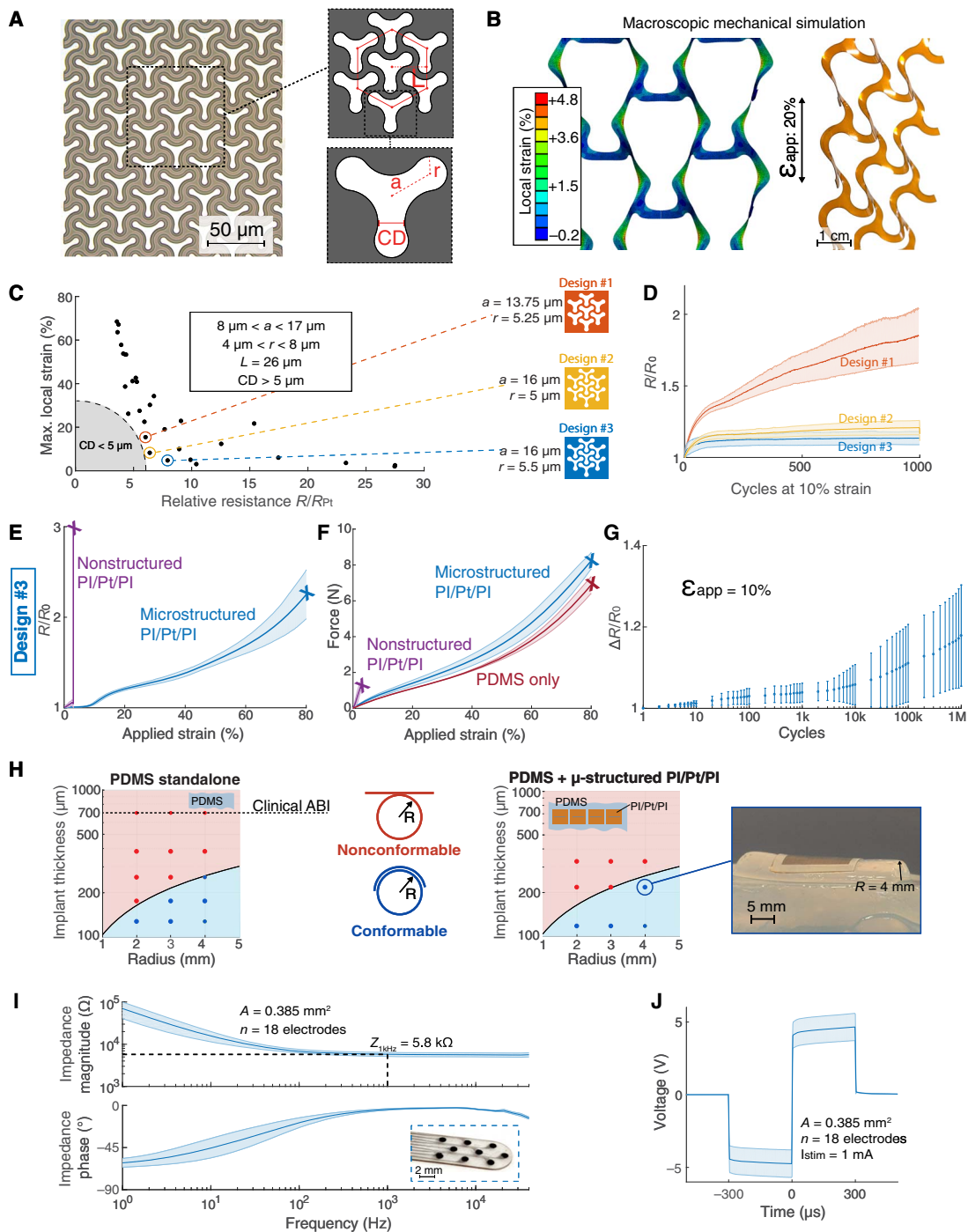
positioning of the soft ABI (Fig. 3D and movie S3). The implant can then be manipulated for about 35 min (in and out of the brainstem region) before the PVA (1 mm thick) softens and eventually dissolves (fig. S18), allowing the soft ABI to match the curvature of the underlying CN (Fig. 3E).

We next assessed the electrochemical stability of the microfabricated electrodes before, during, and after implantation. We found that both the clinical array and soft ABI electrodes displayed higher electrode impedance after surgical insertion (Fig. 3, F and G); this reflects the usual electrode-tissue interface. After explantation, impedances
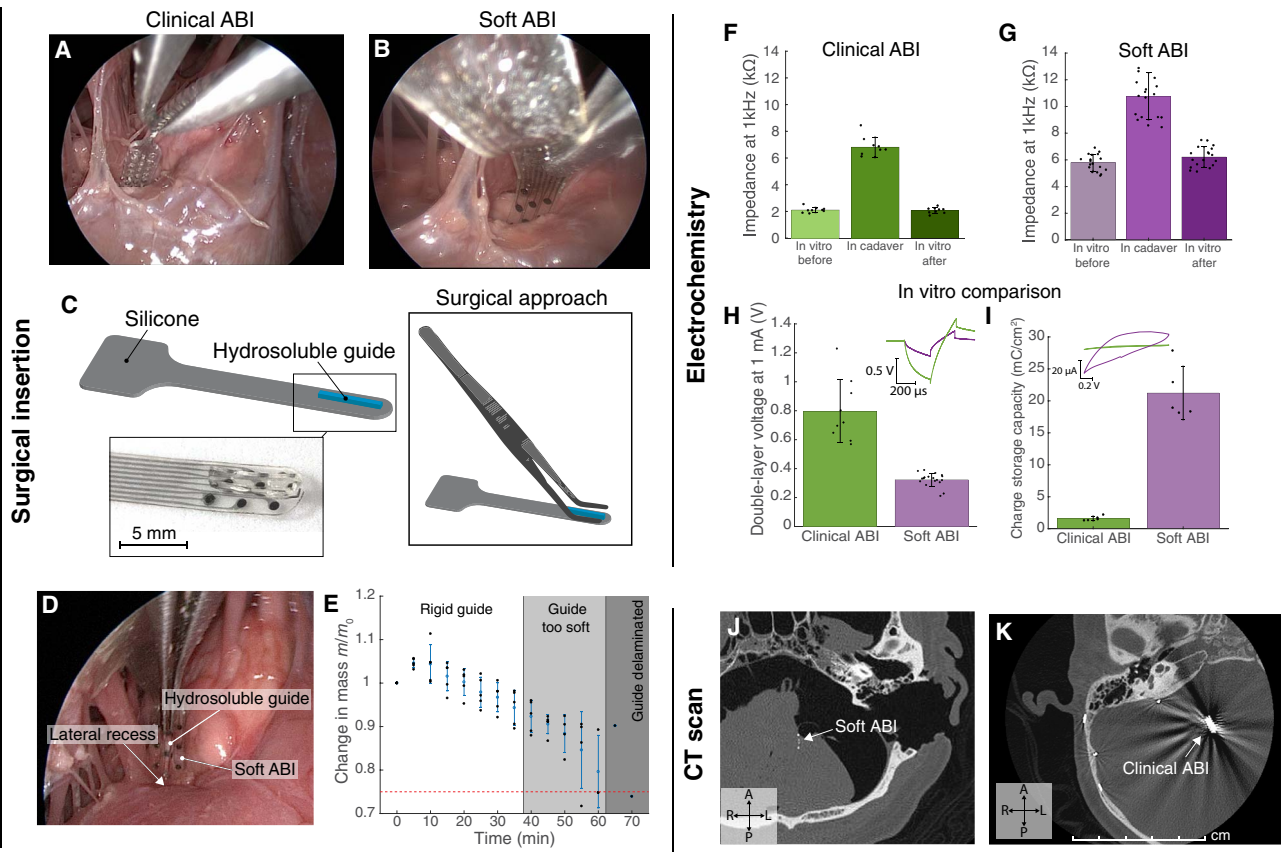
Fig. 3. Comparison of clinical and soft ABI electrode arrays in human cadavers. (**A** and **B**) Endoscopic view of a clinical ABI and soft ABI being inserted in the lateral recess of the fourth ventricle in a human cadaver. (**C**) Schematic (top) and photograph (bottom) of the soft ABI to which a hydrogel guide is glued on the back side of the electrode paddle. To adjust position of the ABI, the guide can be grasped by tweezers (right). (**D**) Endoscopic view of the insertion of the soft ABI with the guide being held by the tweezers. (**E**) Graph of the water mass intake of a mock-up soft ABI with the guide as a function of time ($n = 5$). The red dashed line denotes the moment at which the device is too soft to be inserted in a model of the lateral recess in agarose. (**F** and **G**) Impedance at 1 kHz for the clinical (green, $n = 1$ sample with nine electrodes) and soft (purple, $n = 2$ samples with nine electrodes each) ABIs measured in vitro in PBS before insertion, after insertion in the cadaver, and again in vitro after removal. (**H**) The voltage drop at the electrode interface upon electrical stimulation was extracted from the voltage transients, measured during stimulation, by removing the voltage drop in the interconnects (access resistance). Inset: Examples of voltage drop at the electrode interface for the clinical ABI (green) and the soft ABI (purple). Stimulation was performed with a biphasic symmetrical current pulse of 1 mA for the clinical ABI (green, $n = 1$ sample with nine electrodes) and soft ABI (purple, $n = 2$ sample with nine electrodes each). (**I**) Charge storage capacity extracted from the cyclic voltammogram of the clinical ABI (green) and a soft ABI (purple). $n = 1$ sample with five electrodes each in both cases. Inset: Examples of cyclic voltammograms measured from a clinical ABI (green) and a soft ABI (purple). (**J**) CT scan of the cadaver implanted with a soft ABI, showing almost no artifact. (**K**) CT scan of a pediatric patient with a clinical ABI, showing substantial "windmill" artifact. All bars denote SD. A, anterior; P, posterior; L, left; R, right.

recovered to their preimplantation values, indicating minimal damage to the electrodes from the procedure.

Although the impedance, Z, of the soft ABI electrodes was higher than that of the clinical device ($Z_{1kHz} = 5.78 \pm 0.62$ kilohms, $n = 18$ soft electrodes, geometric surface area = 0.385 mm²; $Z_{1kHz} = 2.11 \pm 0.07$ kilohms, $n = 8$ clinical electrodes, geometric surface area = 0.385 mm²; Fig. 3, H and I), the electrochemical properties of the soft coating at the interface are superior. The double-layer voltage at the electrode-electrolyte interface was 0.80 ± 0.22 V ($n = 18$) for the soft ABI versus 0.32 ± 0.05 V ($n = 9$) for the clinical ABI (Fig. 3H), indicating that the charge injection capacity of the soft ABI was significantly larger than that of the clinical ABI ($P < 0.001$). Furthermore, the charge storage capacity was measured as 21.23 ± 4.19 mC/cm² ($n = 5$) using cyclic voltammetry of the soft ABI in vitro, which was significantly larger ($P = 0.0079$) than that of the clinical ABI (1.60 ± 0.37 mC/cm², $n = 5$) (Fig. 3I). This confirmed that the electrochemical surface area of the

soft coating was larger than that of the flat platinum-iridium electrode used in the clinical ABI. These results indicate that the soft ABI electrodes display a potentially larger dynamic range compared to the clinical ABIs, and the electrode contact may be miniaturized while safely delivering the same amount of charge to the underlying CN.

The soft ABI array also had superior resolution on computed tomography (CT) and MRI; this is mainly enabled by the thinness of the microstructured metallization. A CT scan performed on one of the cadaveric head specimens implanted with the soft ABI showed that the array electrodes are clearly visible without artifacts or distortions in the surrounding brain (Fig. 3J). For comparison, a CT scan image from a pediatric patient implanted with a clinical ABI (Cochlear Ltd.) shows distortions and artifacts around the array (Fig. 3K). MRI also showed an artifact-free soft ABI, whereas the clinical ABI induced artifacts (fig. S19). Endoscopic visualization of the ABI after imaging confirmed that neither array had migrated as a result of these scans.

Chronic evaluation of the soft ABI in a mouse model

Functionality of the soft ABI was tested in chronic conditions in a mouse model. The small size of the mouse DCN surface (~500 μm × 500 μm) required miniaturization of our microstructured interconnects and electrodes to host three electrode sites in the array (fig. S20). Figure 4 (A to D) displays photographs and a schematic view of the mouse auditory pathways, denoting the location of the stimulation and recording electrode arrays. We developed a surgical approach suitable for chronic implantation, on the basis of a double craniotomy through which the array was looped (Fig. 4, B and C, and fig. S21). Access to the DCN required partial removal of the cerebellum. Ten mice were implanted with identical soft ABIs for 4 weeks (experimental timeline shown in Fig. 4E).

Upon implantation, electrode impedances displayed an expected increase in modulus (Fig. 4F). Further plots of impedance at 10 kHz (instead of the typical 1 kHz) were reported, because the impedance at this frequency is much closer to the resistance of the system (the double-layer capacitance being short-circuited at higher frequency) and thus more representative of how much current can be injected before reaching the voltage compliance of the stimulator (12 V), which, in this case study, is the limiting factor for electrical stimulation and not charge injection capacity (Fig. 4G). Over the course of 4 weeks, little further change in impedance at 10 kHz was observed on average, suggesting that both electrodes and interconnects remained stable in vivo. High impedance values (>150 kilohms) were measured intermittently on some electrodes and were mostly artifacts due to a noisy and sensitive measurement setup and the subcutaneous positioning of the counter electrode in the mouse. Some data points were therefore discarded on some days. Overall, most electrodes remained under 80 kilohms, which is the theoretical impedance limit for stimulation at 150 μA with a voltage compliance of 12 V.

In response to electrical stimulation of the array, we recorded electrically evoked auditory brainstem responses (eABRs) at weekly intervals (Fig. 4H). Although there was some variability in waveform, the ABI array elicited robust responses up to the conclusion of the experiment (4 weeks). The eABR traces had larger amplitudes than acoustically evoked ABRs (aABRs) (fig. S22) because the underlying neural activity is less synchronized in response to an acoustic click compared to an electrical pulse. Reduced acoustic synchrony mostly arises because activity is initiated at different times along the cochlea by the frequency-dependent delays of the traveling wave (34, 35).

Recordings from the inferior colliculus (IC) were performed using a commercially available silicon shank that was inserted inside the midbrain on week 0, removed during the implantation period, and reinserted in the IC at week 4. The spike rate computed from IC recordings collected at week 4 was about the same as the rate collected at week 1 (Fig. 4, I and J), although differences in temporal patterns were observed. This difference may have resulted from reinsertion and recording at a slightly different position at week 4 or perhaps from scarring of the brain tissue as a result of the week 0 recording (36). The fact that both eABR and IC neural activity showed robust responses confirmed the functionality of the soft ABI over 4 weeks in chronic conditions in vivo (Fig. 4K).

DISCUSSION

Here, we developed a soft ABI technology designed using materials that allow for ease of surgical insertion and conformability to the curvature of the brainstem. We successfully engineered the elastic microstructured multilayers, soft electrode coating, and transient surgical features that allowed for fabrication of a scalable ABI from miniaturized mouse implants to human-sized arrays. In a human cadaveric model, we demonstrated that the soft ABI is robust to surgical manipulation and insertion into the lateral recess of the fourth ventricle and displayed improved electrochemical performance compared to current clinical devices. In a mouse model, we showed that soft neurotechnology could be implanted to reliably record central auditory neurons in vivo for up to 4 weeks.

The technology used to fabricate our soft ABI is an advance in a number of distinct ways that are essential for the ABI patient population and may help inform implant design for other applications. First, to better withstand implant manipulation during the ABI surgical procedure and the dynamic microenvironment of the brain, we fabricated stretchable interconnects that conferred elasticity to the electrode tracks. We showed that microstructuring interconnects made of PI/Pt/PI with hexagonal arrays of optimized Y-shaped motifs could achieve reversible elasticity for 1 million cycles at 10% elongation, as well as remain electrically and mechanically functional for applied strains up to 70%. This is an improvement compared to nonpatterned tracks that would fail at strains as low as 2 to 3%.

Second, for surgical insertion into the lateral recess, it is important that the array remains transiently stiff to facilitate insertion and enable repositioning of the array if the initial placement is unsatisfactory. To tackle this issue, we developed a hydrosoluble mechanical guide to temporarily stiffen the array. Third, we also incorporated stretchable coatings with high electrochemical area, which allowed us to improve the electromechanical performance of the arrays at the electrode-tissue interface, compared to conventional platinum contacts currently used in ABIs. This technology can potentially allow the use of larger currents for CN stimulation without generating electrolysis around the tissue. Last, the reduced amount of metal in the electrodes makes the soft ABI compatible with conventional clinical imaging techniques (MRI and CT scans), thereby minimizing artifacts that can obscure details about device position as well as surrounding neural anatomy (37–40). This is critical because NF2 patients, the most common patient cohort to receive the ABI, require routine MRI surveillance to detect new tumor growth. Because both monitoring and therapeutic neural implants are used in clinical care, their compatibility with high-resolution imaging techniques is now a prerequisite.

We tested the soft ABIs in human cadavers and a mouse model. It is important to note that the evaluation of the mouse ABI was centered on whether the array was sufficiently durable to continue to stimulate the CN over a 4-week period. However, the number of pulses experienced in our study remains low compared to the billions of pulses that would be required for daily stimulation across decades of use in a human. Further experiments are also necessary to evaluate the influence of device connector fixation and torque of the cable on long-term ABI position as well as the effects of chronic stimulation on the electrode array, because it was only tested here for 4 weeks. Last, evaluation of human-sized soft array requires the more appropriate model of nonhuman primates (NHPs) that have similar anatomy to humans. NHPs have been successfully implanted with an ABI using the same surgical approach used clinically, although the paddle was slightly reduced in size (41). Nevertheless, our mouse ABI model is valuable for initial in vivo evaluation of electrode materials and also represents a good tool to pursue more fundamental research to better understand the mechanisms of CN electrical stimulation.

Vachicouras et al., Sci. Transl. Med. 11, eaax9487 (2019)   16 October 2019

6 of 11

Fig. 4. Chronic functional tests of soft ABI electrode arrays in the mouse. (**A**) Photograph of the mouse ABI and images showing the microstructured tracks. The connector had pins for each of the three electrodes and a fourth pin to allow for control due to artifact stimulation. (**B**) 3D schematic of the ABI, showing the connector on the top of the head and the cable looping through a small posterior craniotomy to access the surface of the DCN as viewed through a second larger craniotomy. (**C**) Right: Surgical image of the ABI and its three electrodes (each of diameter 150 μm) on the surface of the DCN. Left: Illustration of the electrode array on an image of the CN, the latter generated using data of Muniak *et al*. (*48*). (**D**) Electrophysiological setup showing how stimulation of the CN was performed with biphasic current pulses (blue) applied to the electrodes of soft ABI. Responses recorded were (i) auditory brainstem responses (ABRs) recorded using surface electrodes on the vertex and left ear (top left), and (ii) neural responses recorded by a 16-channel penetrating probe in the inferior colliculus (IC), which receives crossing projections from the CN (diagram at right). Acoustic tones were used to calibrate the position of the probe. (**E**) Timeline of experiments. (**F**) Electrochemical impedance spectra (EIS) of electrodes in vitro (blue, *n* = 11), in vivo week 0 (black, *n* = 11), and in vivo week 4 (red, *n* = 12). Error bars denote SEM. (**G**) Mean impedance at 10 kHz (indicating the access resistance) at different time points for all electrodes. Error bars denote SD. Data extracted from four mice (four implants and three electrodes each). (**H**) Example waveforms of electrically evoked ABRs (eABRs) evoked by monopolar electrical stimulation of one electrode in a single mouse. The beginning of the traces (first millisecond) contains electrical stimulation artifacts and thus has been grayed out. (**I**) Example post-stimulus time histogram (PSTH) elicited by monopolar stimulation on week 0. (**J**) PSTH of the same mouse and same stimulation electrode on week 4. (**K**) Curves of IC activity for all stimulation electrodes across all mice. The bold curves show the average for weeks 0 (in black) and 4 (in red). *n* = 3 × 4 = 12. Bars denote SE. L, lateral; M, medial; A, anterior; P, posterior.
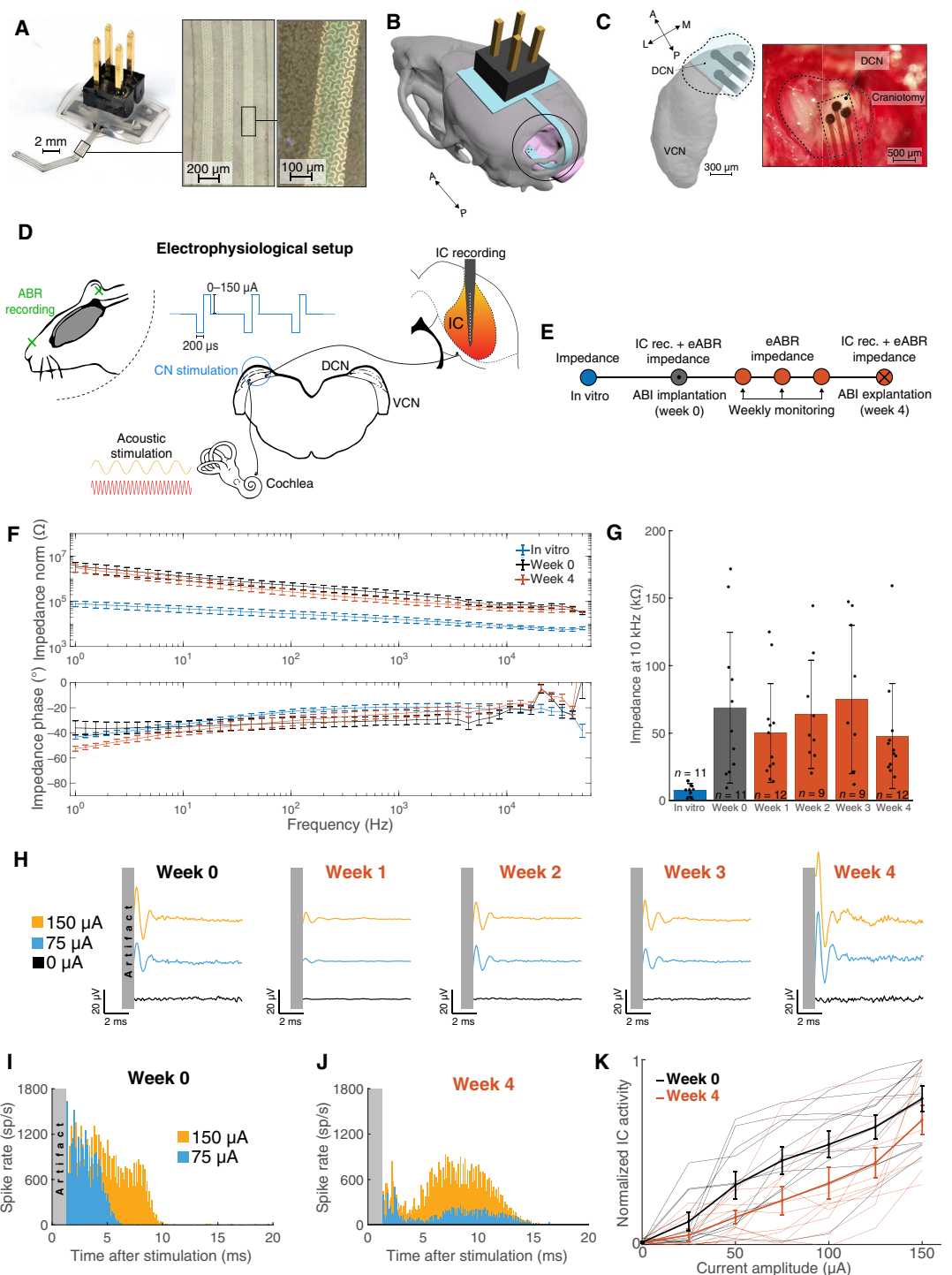
Our studies with the soft ABI in human cadavers provided important insights into feasibility for clinical use and showed how using a temporary guide could ease surgical insertion of the array. However, the technique used for the cadaveric specimens does have a few notable differences from live human surgery, including the absence of brain pulsations, cerebrospinal fluid, and bleeding, as well as a more flattened cerebellum that enables a more direct approach with less retraction. In addition, candidates for ABI surgery often have tumors (vestibular schwannomas), which can deform brainstem anatomy and further complicate surgery. This consideration was not evaluated

Vachicouras *et al*., *Sci. Transl. Med.* **11**, eaax9487 (2019)   16 October 2019

7 of 11

in this work, although the conformability of our implants might compensate for patient-to-patient anatomic variability. Again, a larger animal model, such as NHPs, would aid in better determining the clinical feasibility of using a soft ABI. Preclinical validation would be necessary before moving to testing in a human clinical trial to assess safety and the impact of the soft ABI on sound and speech perception outcomes.

Last, auditory prostheses such as the cochlear implant and ABI, which were some of the earliest and remain among the few FDA-approved implantable neural interfaces for the brain surface, have a long history of paving the way for subsequent implants in other systems. The developments showed in this work could help advance neural interfaces used in other conditions such as epilepsy, Parkinson's disease, motor paralysis, and blindness. Softer materials, stretchable interconnects, temporary rigidification, and reduced metallic artifact in imaging represent potential advances for all of these existing implants and may also ultimately enable novel applications in regions of the brain that are otherwise inaccessible with existing rigid implants. Our soft neurotechnology is versatile and can be optimized and tailored to modulate responses of the auditory cortex (42) or auditory midbrain (43) for restoring hearing or the caudate nucleus to suppress tinnitus (44).

MATERIALS AND METHODS
Study design
The main hypothesis of this study was that a soft ABI could enhance biomechanical compatibility with the curved CN surface. Our first objective was to define the materials and design to manufacture a device that was soft enough that it could conform to the curvature of the human CN while being electromechanically resilient to the surgical implantation. Our second objective was to assess the feasibility of surgically implanting a soft ABI into the lateral recess of the fourth ventricle. Last, our third objective was to elucidate the possibility of functional activation of the auditory pathways upon electrical stimulation of the mouse CN with a miniaturized soft ABI using the same technology. All in vivo studies were performed in accordance with the National Institutes of Health *Guide for the Care and Use of Laboratory Animals* as well as approved by the Massachusetts Eye and Ear Infirmary Animal Care committee (Boston, MA; protocol no. 09-07-015A).

Electromechanical characterization of the stretchable interconnects was performed upon cyclic elongation on $n = 8$ tracks; elongation until break was recorded across $n = 16$ tracks. Electrochemical characterization of the soft ABI electrodes in vitro and in the cadaver was performed on $n = 18$ electrodes, and on $n = 9$ electrodes for the clinical ABI. Dissolution rates of the hydrosoluble guide were performed on $n = 5$ samples. In vivo experiments were performed on $n = 4$ mice, and electrode functionality and electrochemical characterization in vivo was performed on a total of $n = 12$ electrodes. Experiments and data analysis were not blinded.

DCN curvature estimation from histological specimens
This study was approved by the institution's Human Studies Committee (no. 1447618, exempt). Postmortem human brainstem sections of the left CN from three healthy adult individuals were used for histological reconstructions. Axial brainstem sections 10 to 20 μm in thickness were stained with protargol, cresyl violet (Nissl stain), or hematoxylin.

The CN was identified using light microscopy, and its borders were manually traced in each relevant section. Laterality selection (left ver-

sus right) was based on overall ease of CN identification and quality of preservation in sections. Sections were aligned using vessels, histologic artifacts, and other features that remained consistent between sections. The DCN trace was isolated and imported into MATLAB (MathWorks) for further curvature analysis. The trace of the DCN from histological reconstructions was fitted with a circle using a previously proposed method for circle fitting of a cloud of points in a 2D plane (45).

The CN was successfully extracted from human brain histological slices (fig. S17), and the average radius of curvature of the DCN across specimens ($n = 3$) and histological slices was, on average, 2.85 ± 0.5 mm ($n = 3$). It was noticed that the DCN radius of curvature in histological specimens was underestimated. Only the MRI radiological reconstruction showed that the radius of curvature was actually larger ($r \approx 8$ mm). This makes sense, as histological slices tend to shrink the anatomical structures as the tissues are dry and no longer contain CSF (cerebrospinal fluid), for example.

On the basis of the calculations of curvature above, the radius of curvature of the CN was defined at 2.85 mm, knowing that this was a very conservative value. Thus, the maximum thickness for a sheet of PDMS to conform by capillarity to a cylinder of 2.85 mm in radius was defined using the equations from the "Conformability of film on wet cylinder" section in the Supplementary Materials. For a cylinder of radius 2.85 mm, with the surface tension of cerebrospinal fluid at 22°C ($\gamma = 61.55$ mJ/m^2) (46) and to a substrate of PDMS ($E = 1$ MPa and $\nu = 0.49$) (47), the calculated theoretical maximum thickness for the ABI can be 210 μm. It was therefore decided to fabricate the soft ABI with an approximate total target thickness of 200 μm, knowing that, in reality, the radius of curvature of the DCN was larger, due to it being soaked in cerebrospinal fluid.

Mouse experiments
Husbandry and surgical approach
All experimental procedures were performed in accordance with the National Institutes of Health *Guide for the Care and Use of Laboratory Animals* as well as approved by the Massachusetts Eye and Ear Infirmary Animal Care committee (Boston, MA; protocol no. 09-07-015A). Ten CBA/CaJ mice (three females and seven males) were used in this study. Mouse age ranged from 5 to 18 weeks and weights were between 20 and 40 g. Only five mice survived the complete 4-week experiment. One mouse was discarded from the experiment because the connector failed and the electrodes were nonfunctional after 4 weeks, so a total of four mice provided data.

Mice were anesthetized with an intraperitoneal systemic injection of ketamine (20%) (diluted in saline, injection of 0.5 ml/g) and xylazine (10%) (diluted in saline, injection of 0.5 ml/g). During the surgical procedure, supplementary doses of ketamine (70% of the initial ketamine dose) were injected when required as determined on the base of paw pinch reflex. The surgery and remainder of the experiments were performed within an electrically and acoustically isolated chamber. After anesthesia, the mouse was shaved and positioned in a stereotaxic instrument. The temperature of the mouse was kept at 37°C with a heating pad. The heating pad was disconnected during recordings to avoid noise from the power network. A midline incision of the skin was created, and the skin was removed to expose the caudal part of the skull, where overlying muscles were removed to expose the left occipital bone. A double occipital craniotomy was performed, and a portion of the lateral cerebellum was aspirated to expose the left CN (fig. S21, A and B). Using a surgical blade, a rectangular craniotomy was then

performed on the contralateral (right) side rostrally from the right lambdoid suture over the IC (fig. S21D).

Auditory brainstem responses

ABRs were recorded differentially using subcutaneous needles inserted below the ipsilateral ear pinna, on the vertex of the mouse's head, with a reference on the back of the mouse. A preamplifier (Model 1201 Low Noise Voltage Preamplifier, DL Instruments) with a gain of 10,000 and a bandpass filter (300 Hz to 3 kHz, five-pole) situated inside the chamber was connected to a computer situated outside. Data were acquired at a sampling frequency of 2 or 20 kHz and averaged across 512 trials for a duration of 15 ms.

aABRs were evoked by clicks (0 to 80 dB in steps of 20 dB) produced by a custom-made earphone inserted in the left ear canal. These aABRs confirmed that the mouse had normal thresholds (fig. S22). eABRs were recorded similarly in response to electrical stimulation of the CN with the ABI electrodes. These eABR recordings were performed each week.

IC neural recordings

Recordings of IC multiunit neural activity were performed with a 16-channel ($\oslash$ = 50 μm) linear penetrating electrode array (A1x16-3mm-50-177-A16, NeuroNexus Technologies). The probe was held by a stereotaxic aligner and inserted on the dorso-ventral direction in the cerebellum such that it accessed the tonotopic organization of the IC. The 16-channel IC probe was connected to a preamplifier (Plexon PBX3/16spr-G1000) with a gain of 1000 and a bandpass filter (150 Hz, one pole; 8 kHz, three poles). Data acquired at a sampling frequency of fs = 25 kHz from all 16-channels were transferred to a computer located outside the anechoic chamber. The recordings lasted 30 ms post-stimulation and were averaged (20 averages) for each channel. A global reference was used for all electrodes with a subcutaneous wire inserted near the mouse neck.

To confirm the location of the IC probe, acoustic tones were generated at various frequencies (8 to 45.25 kHz, in steps of one-half octaves) and at various intensities (from 0 to 80 dB in 20 dB steps) in the left ear, while the IC activity (root mean square of the IC recording) was recorded using custom-made software on each of the 16 channels. The IC electrode placement was confirmed by observing a tonotopic shift along the probe channels as the frequency of the acoustic stimuli increased.

IC recordings were then performed in response to electrical stimulation at week 0 (intraoperatively), the IC probe was removed, and the IC craniotomy was covered with quick-seal. The IC craniotomy was opened up again 4 weeks later to perform a final recording session, by implanting again the IC probe, following the same procedure as described above.

ABI implantation and electrical stimulation in mice

The mouse ABI was placed onto the DCN, and its wire connections were looped through a small adjacent craniotomy to provide stability (fig. S21C). A muscle plug was used to keep the ABI in place. After the stimulation/recording session, at week 0, the ABI was fixated with dental cement on the skull. Electrical current was provided by a custom-made stimulator using either monopolar or bipolar stimulation (for monopolar stimulation, the same ground as the IC recording probe was used). Trains of biphasic symmetrical pulses (the polarity of each pulse was alternated) were at a rate of 23 pulses/s. Each phase lasted 200 μs, and the current amplitude ranged from 0 to 150 μA with steps of 25 μA. Each pulse train lasted 0.5 s and was followed by an off period of 0.5 s, for a comparison to baseline (14 pulses per train). Each of these pulse trains was repeated in total 30 times for each current amplitude [420 (14 × 30) stimulation

pulses per current amplitude]. The amplitude order of each pulse train was chosen randomly by a computer. During stimulation, eABRs and IC recordings were performed simultaneously for a period of 15 ms after the end of the stimulation pulse.

In addition to the three electrodes of the soft ABI, a fourth contact pin was included in the head connector of all mice and was not connected to any electrode. It was used as a control pin to confirm that observed spikes in recordings were not generated by electrical stimulation artifacts (fig. S23).

Data processing of mouse electrophysiology

aABR recordings were averaged across 512 trials and were reported without any additional post-processing. eABR recordings were averaged across 430 trials and filtered with a low-pass Butterworth filter (order 5, f_c = 3 kHz).

IC recordings were first filtered with a Butterworth high-pass filter (order 5, f_c = 500 Hz) and a low-pass filter (order 5, f_c = 3000 Hz). Spike detection was then performed using a threshold of three times the standard deviation of the filtered baseline signal (recordings without any stimulation). The IC spike rate was calculated on a 0.1-ms sliding window. IC spike rate during baseline (spontaneous activity) was subtracted from the IC spike rate during electrical stimulation. Post-stimulus time histograms (PSTHs) were then generated to show the evolution of the spike rate as a function of time. The spike rates during the first 1.2 ms were ignored due to stimulation artifacts. All PSTHs extracted for the four mice using each electrodes are shown in fig. S24 at weeks 0 and 4.

IC activity a_{IC} was defined as the integral of IC spike rate during the first 10 ms for a given stimulation amplitude:

$$a_{IC} = \int_0^{10ms} PSTH(t) \, dt$$

The IC activity was normalized for each mouse by dividing it by the highest IC activity observed in a mouse across all stimulation electrodes and recording sessions (weeks 0 and 4).

Statistical analysis

Data were tested for normality using the Lilliefors test and then analyzed statistically with a paired t test or Wilcoxon rank sum test as required. Significant effects were reported for $P < 0.05$.

SUPPLEMENTARY MATERIALS

Vachicouras et al., Sci. Transl. Med. 11, eaax9487 (2019)   16 October 2019

9 of 11

View/request a protocol for this paper from *Bio-protocol*.

REFERENCES AND NOTES

1. W. F. House, W. E. Hitselberger, Twenty-year report of the first auditory brain stem nucleus implant. *Ann. Otol. Rhinol. Laryngol.* **110**, 103–104 (2016).
2. C. Vincent, Auditory brainstem implants: How do they work? *Anat. Rec.* **295**, 1981–1986 (2012).
3. V. Colletti, R. Shannon, M. Carner, S. Veronese, L. Colletti, Outcomes in nontumor adults fitted with the auditory brainstem implant: 10 years' experience. *Otol. Neurotol.* **30**, 614–618 (2009).
4. K. S. Noij, E. D. Kozin, R. Sethi, P. V. Shah, A. B. Kaplan, B. Herrmann, A. Remenschneider, D. J. Lee, Systematic review of nontumor pediatric auditory brainstem implant outcomes. *Otolaryngol. Head Neck Surg.* **153**, 739–750 (2015).
5. T. K. Chao, B. J. Burgess, D. K. Eddington, J. B. Nadol Jr., Morphometric changes in the cochlear nucleus in patients who had undergone cochlear implantation for bilateral profound deafness. *Hear. Res.* **174**, 196–205 (2002).
6. H. L. Seldon, G. M. Clark, Human cochlear nucleus: Comparison of Nissl-stained neurons from deaf and hearing patients. *Brain Res.* **551**, 185–194 (1991).
7. M. C. Brown, A. M. Berglund, N. Y. S. Kiang, D. K. Ryugo, Central trajectories of type II spiral ganglion neurons. *J. Comp. Neurol.* **278**, 581–590 (1988).
8. E. M. Rouiller, R. Cronin-Schreiber, D. M. Fekete, D. K. Ryugo, The central projections of intracellularly labeled auditory nerve fibers in cats: An analysis of terminal morphology. *J. Comp. Neurol.* **249**, 261–278 (1986).
9. M. S. Schwartz, S. R. Otto, R. V. Shannon, W. E. Hitselberger, D. E. Brackmann, Auditory brainstem implants. *Neurotherapeutics* **5**, 128–136 (2008).
10. S. R. Barber, E. D. Kozin, A. K. Remenschneider, S. V. Puram, M. Smith, B. S. Herrmann, M. E. Cunnane, M. C. Brown, D. J. Lee, Auditory brainstem implant array position varies widely among adult and pediatric patients and is associated with perception. *Ear Hear.* **38**, e343–e351 (2017).
11. V. Colletti, Auditory outcomes in tumor vs. nontumor patients fitted with auditory brainstem implants. *Adv. Otorhinolaryngol.* **64**, 167–185 (2006).
12. I. R. Minev, N. Wenger, G. Courtine, S. P. Lacour, Research Update: Platinum-elastomer mesocomposite as neural electrode coating. *APL Mater.* **3**, 014701 (2015).
13. J. H. Lee, H. Kim, J. H. Kim, S.-H. Lee, Soft implantable microelectrodes for future medicine: Prosthetics, neural signal recording and neuromodulation. *Lab Chip* **16**, 959–976 (2016).
14. J.-W. Jeong, G. Shin, S. I. Park, K. J. Yu, L. Xu, J. A. Rogers, Soft materials in neuroengineering for hard problems in neuroscience. *Neuron* **86**, 175–186 (2015).
15. M. E. Wagshul, P. K. Eide, J. R. Madsen, The pulsating brain: A review of experimental and clinical studies of intracranial pulsatility. *Fluids Barriers CNS* **8**, 5 (2011).
16. D. S. Gray, J. Tien, C. S. Chen, High-conductivity elastomeric electronics. *Adv. Mater.* **16**, 393–397 (2004).
17. M. Gonzalez, F. Axisa, M. Vanden Bulcke, D. Brosteaux, B. Vandevelde, J. Vanfleteren, in *2007 International Conference on Thermal, Mechanical and Multi-Physics Simulation Experiments in Microelectronics and Micro-Systems. EuroSime 2007* (IEEE, 2007), pp. 1–6.
18. X. Ning, X. Wang, Y. Zhang, X. Yu, D. Choi, N. Zheng, D. S. Kim, Y. Huang, Y. Zhang, J. A. Rogers, Assembly of advanced materials into 3D functional structures by methods inspired by origami and kirigami: A review. *Adv. Mater. Interfaces* **5**, 1800284 (2018).
19. F. Xu, Y. Zhu, Highly conductive and stretchable silver nanowire conductors. *Adv. Mater.* **24**, 5117–5122 (2012).
20. S. M. Won, E. Song, J. Zhao, J. Li, J. Rivnay, J. A. Rogers, Recent advances in materials, devices, and systems for neural interfaces. *Adv. Mater.* **30**, 1–19 (2018).
21. A. Lecomte, E. Descamps, C. Bergaud, A review on mechanical considerations for chronically-implanted neural probes. *J. Neural Eng.* **15**, 031001 (2018).
22. S. M. Wellman, J. R. Eles, K. A. Ludwig, J. P. Seymour, N. J. Michelson, W. E. McFadden, A. L. Vazquez, T. D. Y. Kozai, A materials roadmap to functional neural interface design. *Adv. Funct. Mater.* **28**, 1–38 (2018).
23. J. Viventi, D.-H. Kim, J. D. Moss, Y.-S. Kim, J. A. Blanco, N. Annetta, A. Hicks, J. Xiao, Y. Huang, D. J. Callans, J. A. Rogers, B. Litt, A conformal, bio-interfaced class of silicon electronics for mapping cardiac electrophysiology. *Sci. Transl. Med.* **24**, 24ra22 (2010).
24. D. Khodagholy, J. N. Gelinas, T. Thesen, W. Doyle, O. Devinsky, G. G. Malliaras, G. Buzsáki, NeuroGrid: Recording action potentials from the surface of the brain. *Nat. Neurosci.* **18**, 310–315 (2015).
25. J. Ordonez, M. Schuettler, C. Boehler, T. Boretius, T. Stieglitz, Thin films and microelectrode arrays for neuroprosthetics. *MRS Bull.* **37**, 590–598 (2012).
26. J. S. Ordonez, C. Boehler, M. Schuettler, T. Stieglitz, Improved polyimide thin-film electrodes for neural implants. *Conf. Proc. IEEE Eng. Med. Biol. Soc.*, 5134–5137 (2012).
27. F. Ceyssens, R. Puers, Insulation lifetime improvement of polyimide thin film neural implants. *J. Neural Eng.* **12**, 054001 (2015).
28. T. L. Edwards, C. L. Cottriall, K. Xue, M. P. Simunovic, J. D. Ramsden, E. Zrenner, R. E. MacLaren, Assessment of the electronic retinal implant Alpha AMS in restoring vision to blind patients with end-stage retinitis pigmentosa. *Ophthalmology* **125**, 432–443 (2018).
29. S. Raspopovic, M. Capogrosso, F. M. Petrini, M. Bonizzato, J. Rigosa, G. Di Pino, J. Carpaneto, M. Controzzi, T. Boretius, E. Fernandez, G. Granata, C. M. Oddo, L. Citi, A. L. Ciancio, C. Cipriani, M. C. Carrozza, W. Jensen, E. Guglielmelli, T. Stieglitz, P. M. Rossini, S. Micera, Restoring natural sensory feedback in real-time bidirectional hand prostheses. *Sci. Transl. Med.* **6**, 222ra19 (2014).
30. Cochlear Americas, *Summary of Safety and Effectiveness-Auditory Brainstem Implant* (2000); https://www.accessdata.fda.gov/scrlpts/cdrh/cfdocs/cfpma/pma.cfm?id=P000015.
31. N. Vachicouras, C. M. Tringides, P. B. Campiche, S. P. Lacour, Engineering reversible elasticity in ductile and brittle thin films supported by a plastic foil. *Extreme Mech. Lett.* **15**, 63–69 (2017).
32. S. P. Lacour, S. Wagner, Z. Huang, Z. Suo, Stretchable gold conductors on elastomeric substrates. *Appl. Phys. Lett.* **82**, 2404–2406 (2003).
33. ISO 45502-2-3:2010, Active implantable medical devices. Particular requirements for cochlear and auditory brainstem implant systems (2010).
34. T. Dau, O. Wegner, V. Mellert, B. Kollmeier, Auditory brainstem responses with optimized chirp signals compensating basilar-membrane dispersion. *J. Acoust. Soc. Am.* **107**, 1530–1540 (2000).
35. M. C. Brown, The antidromic compound action potential of the auditory nerve. *J. Neurophysiol.* **71**, 1826–1834 (1994).
36. K. A. Potter, A. C. Buck, W. K. Self, J. R. Capadona, Stab injury and device implantation within the brain results in inversely multiphasic neuroinflammatory and neurodegenerative responses. *J. Neural Eng.* **9**, 046020 (2012).
37. P. Serano, L. M. Angelone, H. Katnani, E. Eskandar, G. Bonmassar, A novel brain stimulation technology provides compatibility with MRI. *Sci. Rep.* **5**, 9805 (2015).
38. F. M. Martínez Santiesteban, S. D. Swanson, D. C. Noll, D. J. Anderson, Magnetic resonance compatibility of multichannel silicon microelectrode systems for neural recording and stimulation: Design criteria, tests, and recommendations. *IEEE Trans. Biomed. Eng.* **53**, 547–558 (2006).
39. J. Brian M. Dale, Mark A. Brown, Richard C. SemelkaDurek, *MRI: Basic Principles and Applications* (John Wiley & Sons Ltd., ed. 5, 2015).
40. J. B. Erhardt, E. Fuhrer, O. G. Gruschke, J. Leupold, M. C. Wapler, J. Hennig, T. Stieglitz, J. G. Korvink, Should patients with brain implants undergo MRI? *J. Neural Eng.* **15**, 041002 (2018).
41. Z.-M. Wang, Z.-J. Yang, F. Zhao, B. Wang, X.-C. Wang, P.-R. Qu, P.-N. Liu, Auditory rehabilitation in rhesus macaque monkeys (*Macaca mulatta*) with auditory brainstem implants. *Chin. Med. J.* **128**, 1363–1369 (2015).
42. D. De Ridder, S. Vanneste, S. Kovacs, S. Sunaert, T. Menovsky, P. van de Heyning, A. Moller, Transcranial magnetic stimulation and extradural electrodes implanted on secondary auditory cortex for tinnitus suppression. *J. Neurosurg.* **114**, 903–911 (2011).
43. H. H. Lim, T. Lenarz, Auditory midbrain implant: Research and development towards a second clinical trial. *Hear. Res.* **322**, 212–223 (2015).
44. P. L. Perez, S. S. Wang, S. Heath, J. Henderson-Sabes, D. Mizuiri, L. B. Hinkley, S. S. Nagarajan, P. S. Larson, S. W. Cheung, Human caudate nucleus subdivisions in tinnitus modulation. *J. Neurosurg.* **2019**, 1–7 (2019).
45. I. Bucher, Circle fit*MATLAB* (1991).
46. A. Kratochvíl, E. Hrnčíř, Correlations between the cerebrospinal fluid surface tension value and 1. Concentration of total proteins 2. Number of cell elements. *Gen. Physiol. Biophys.* **21**, 47–53 (2002).
47. C. Py, P. Reverdy, L. Doppler, J. Bico, B. Roman, C. N. Baroud, Capillarity induced folding of elastic sheets. *Eur. Phys. J. Spec. Top.* **166**, 67–71 (2009).
48. M. A. Muniak, A. Rivas, K. L. Montey, B. J. May, H. W. Francis, D. K. Ryugo, 3D model of frequency representation in the cochlear nucleus of the CBA/J mouse. *J. Comp. Neurol.* **521**, 1510–1532 (2013).

Vachicouras *et al.*, *Sci. Transl. Med.* **11**, eaax9487 (2019)   16 October 2019

10 of 11

49. F. Lüsebrink, A. Sciarra, H. Mattern, R. Yakupov, O. Speck, T_1-weighted in vivo human whole brain MRI dataset with an ultrahigh isotropic resolution of 250 μm. *Sci. Data* **4**, 170032 (2017).

50. J. Buhlmann, L. Hofmann, P. A. Tass, C. Hauptmann, Modeling of a segmented electrode for desynchronizing deep brain stimulation. *Front. Neuroeng.* **4**, 15 (2011).

51. M. Ying, A. P. Bonifas, N. Lu, Y. Su, R. Li, H. Cheng, A. Ameen, Y. Huang, J. A. Rogers, Silicon nanomembranes for fingertip electronics. *Nanotechnology* **23**, 344004 (2012).

52. D. Wu, Y. Luo, X. Zhou, Z. Dai, B. Lin, Multilayer poly(vinyl alcohol)-adsorbed coating on poly(dimethylsiloxane) microfluidic chips for biopolymer separation. *Electrophoresis* **26**, 211–218 (2005).

Science Translational Medicine

Microstructured thin-film electrode technology enables proof of concept of scalable, soft auditory brainstem implants

Nicolas Vachicouras, Osama Tarabichi, Vivek V. Kanumuri, Christina M. Tringides, Jennifer Macron, Florian Fallegger, Yohann Thenaisie, Lorenz Epprecht, Stephen McInturff, Ahad A. Qureshi, Valentina Paggi, Martin W. Kuklinski, M. Christian Brown, Daniel J. Lee and Stéphanie P. Lacour

Beneficial bending

Some people with deafness receive auditory brainstem implants (ABIs), neurotechnology that directly stimulates the cochlear nucleus (CN). Unfortunately, auditory outcomes after implantation are limited, possibly due to mismatch between the stiffness of the implant and the CN. Vachicouras *et al.* developed ABIs that conform to the curvature of the CN. The soft arrays could be easily handled during surgery and functioned over 1 month when implanted in mice. A scaled-up version of the conformable ABIs inserted in human cadavers showed good electromechanical and electrochemical stability and a potentially larger dynamic range compared to the clinical ABIs. These proof-of-concept results support further testing in models of deafness.

ARTICLE TOOLS	http://stm.sciencemag.org/content/11/514/eaax9487
SUPPLEMENTARY MATERIALS	http://stm.sciencemag.org/content/suppl/2019/10/11/11.514.eaax9487.DC1
RELATED CONTENT	http://stm.sciencemag.org/content/scitransmed/6/222/222ra19.full http://stm.sciencemag.org/content/scitransmed/6/255/255ra133.full http://stm.sciencemag.org/content/scitransmed/6/257/257ra138.full http://stm.sciencemag.org/content/scitransmed/2/24/24ra22.full http://stm.sciencemag.org/content/scitransmed/10/449/eaao0540.full http://stm.sciencemag.org/content/scitransmed/12/546/eaay9101.full http://stm.sciencemag.org/content/scitransmed/12/553/eabb8086.full
REFERENCES	This article cites 46 articles, 1 of which you can access for free http://stm.sciencemag.org/content/11/514/eaax9487#BIBL
PERMISSIONS	http://www.sciencemag.org/help/reprints-and-permissions

Use of this article is subject to the Terms of Service